Supplementary Material

Stabilizing Pure Phase of $FAPbI_3$ Perovskite Enabled by Solid-Liquid Low Entropy Ink

Kaiyu Wang,[1] Guang Yang,[1] Yuan Jiang,[2] Han Qin,[1] Jianbing Zhu,[1] Xueqin Ran,[1] Yingdong Xia,[1] Lingfeng Chao,[1*] Xiaozheng Duan,[2,3*] Yonghua Chen[1*]

[1]State Key Laboratory of Flexible Electronics (LoFE) & Institute of Advanced Materials (IAM), School of Flexible Electronics (Future Technologies), Nanjing Tech University (NanjingTech), Nanjing 211816, China.

[2]State Key Laboratory of Polymer Science and Technology, Changchun Institute of Applied Chemistry, Chinese Academy of Sciences, Changchun 130022, P. R. China.

[3]School of Applied Chemistry and Engineering, University of Science and Technology of China, Hefei 230026, China.

Kaiyu Wang and Guang Yang contribute equally.

*Corresponding author. Email: iamlfchao@njtech.edu.cn (L.C.); xzduan@ciac.ac.cn (X.D.); iamyhchen@njtech.edu.cn (Y.C.)

Materials and Methods

Materials

Lead iodide (PbI_2, 99.99%) was purchased from TCI. 2,2',7,7'-tetrakis (N,N-di-pmethoxyphenylamine)-9,9'-spirobifluorene (Spiro-OMeTAD) was purchased Youxuan Tech, China. Formamidinium iodide (FAI) was purchased from Great Solar Australia Pty Ltd. Formamidine acetate (FAAc), Chlorobenzene (CB, anhydrous), N, N-dimethylformamide (DMF, anhydrous), 2-Methoxyethanol (2-Me), bis(trifluoromethane)sulfonimide lithium salt (Li-TFSI), 4-tertbutyl-pyridine (tBP) and Potassium chloride (KCl) were purchased from Sigma-Aldrich. Tin oxide (SnO_2) colloid precursor was purchased from Alfa Aesar. 2-(Cyclohex-1-en-1-yl)ethan-1-aminium Iodide (CHEAI) was purchased from SuZhou LiWei Tech Co., Ltd. All the materials were used without further purification.

Precursor solution preparation

Control ink was prepared by dissolving 0.98 mmol FAI, 1.08 mmol PbI_2 and 0.06 mmol FACl in 1 ml DMF. LEI was prepared by dissolving 0.98 mmol FAI, 1.08 mmol PbI_2, 0.06 mmol FACl in the mixed solvent of 1 mL 2-Me and 0.5mmol FAAc.

The Spiro-OMeTAD solution was prepared by dissolving 73.2 mg Spiro-OMeTAD in 1 ml CB, adding 17.5 μL Li-TFSI/ACN solution (520 mg mL^{-1}) and 28.6 μL tBP.

Small-size perovskite solar cell fabrication

FTO substrates were ultrasonically cleaned sequentially in deionized water and isopropanol for 30 min each, and dried using a compressed nitrogen gun. After a 30-min UV-Ozone surface treatment, a SnO_2 electron transport layer (ETL) was deposited by spin-coating a 1:3 diluted SnO_2 nanoparticle water solution at 4000 rpm for 30 s, followed by annealing at 150 °C for 20 min in air. Subsequently, a thin KCl layer was deposited by spin-coating a deionized aqueous solution dissolved with 1 mg mL^{-1} KCl solution at 3000 rpm for 30 s and annealed at 100 °C for 10 min in air. For the blade-coating perovskite thin film, 8 μL of perovskite precursor solution were drop-`cast onto the SnO_2/FTO substrate at a speed of 50 mm s^{-1} in ambient air. The relative humidity was maintained below 30% and the ambient temperature was controlled

at 25 °C during coating to ensure good reproducibility and suppress moisture-induced degradation. All device fabrication steps were performed in a cleanroom environment with a cleanliness level of Class-10000, which effectively minimizes particulate contamination during film formation and device assembly. The films were vacuum flashed for 60 s. For the vacuum annealing process, the chamber was evacuated using a mechanical pump with a nominal pumping speed of 5 $m^3 \cdot h^{-1}$ and a base pressure of approximately 10 Pa was typically reached within 2 s. Then, a pre-annealing step was performed at 90 °C for 10 s, followed by annealing at 145 °C for 15 min. Then, a 1.5 mg mL^{-1} CHEAI solution in IPA was spin-coated onto the perovskite surface at 3,000 rpm and annealed at 100 °C for 1 min. After cooling the film to room temperature, the Spiro-OMeTAD solution was spin-coated on the perovskite thin film at 3000 rpm for 30 s. Finally, an 80-nm thick gold layer was deposited by thermal evaporation to complete the whole device.

Perovskite solar mini-module fabrication: 5 cm × 5 cm.

The modules consisted of 6 solar cells connected in series using interconnects P1, P2, and P3 laser structuring, respectively (Fig. S19). The P1 line is etched on the FTO electrode to define individual cell units. The P2 channel, serving as the interconnection for series connection of cells, is etched after the Spiro-OMeTAD oxidation is completed, ensuring effective electrical connections between each cell unit. The P3 scribe is then performed after all preceding steps are completed, further dividing the device to form the final independent modules. It was then cleaned and deposited with an SnO_2 layer as described above. The large-area perovskite thin films were prepared by the blade coating of the perovskite precursors, and subjected to a vacuum-flash process and subsequent annealing. A 20~30 μL droplet of perovskite precursor was added into the gap (~150 μm) between the blade and substrate, and then the blade was moved on with a speed of ~50 mm s^{-1}. Other procedures were consistent with small-size perovskite solar cells.

Molecular Dynamics Simulation

The coarse-grained MD (Molecular Dynamics) simulations are further applied to explore the microstructural features of PbI_2/FAI precursor solutions with DMF and 2-Me as the solvents.

Herein, the coarse-grained model is constructed based on our previous simulations[1-11] and relative Ref.[12]. The MD simulations are performed using the LAMMPS (Large-scale Atomic/Molecular Massively Parallel Simulator) software[13], assisted by Automated High-Throughput Simulation and Analysis Platform (AHSAP).

In our simulations, the Pb^{2+} ions, I^- ions, FA^+ ions, Ac^- ions, DMF solvent molecules and 2-Me solvent molecules are coarse-grained as single spherical particles (Fig. 2a, b), with the sizes as 2.0 Å, 4.12 Å, 5.6 Å, 4.82 Å, 5.0 Å and 5.0 Å, respectively. These particles are classified as charged, apolar and polar ones[12]. The shifted and truncated LJ (Lennard-Jones) potential used to account for the van der Waals interactions between different particles,

$$U_{LJ}(r) = \begin{cases} 4\varepsilon_{\mathrm{LJ}}\left[\left(\frac{\sigma}{r}\right)^{12} - \left(\frac{\sigma}{r}\right)^{6} + S\right], r \le r_c \\ 0, r > r_c \end{cases} \quad (1)$$

where the energetic parameter is adjusted as $\varepsilon_{\mathrm{LJ}} = 1.0 \sim 2.5$ (which corresponds to 1.0 $k_{\mathrm{B}}T \sim 2.5$ $k_{\mathrm{B}}T$ at $T = 298$ K) and the cutoff is varied in the scope of $r_{\mathrm{c}} = 2^{1/6} \sim 2.5\sigma$[12]. The electrostatic interactions between the ionic particles are taken into account via Coulomb potential calculated by the PPPM (particle-particle-particle-mesh) algorithm[14] with an accuracy of 10^{-5},

$$U_{\mathrm{Coul}} = \frac{Z_i Z_j e^2}{4\pi\varepsilon_0\varepsilon_r r} \quad (2)$$

in which Z_1 and Z_2 denote the valences of the ionic particles i and j, e represents the elementary charge, ε_0 indicates the vacuum permittivity, and the relative dielectric constant of the solutions is set as $\varepsilon_r = 20$.

The simulations are conducted in the canonical (NVT) ensemble and the three-dimentional periodic boundary conditions are applied. The system temperature is controlled using the Langevin thermostat at the room temperature (298K) and the MD time step is fixed as 0.005 (equivalent to 6 fs). The size of the simulation box is fixed as $L^3 = (10.8\mathrm{nm})^3$. In the case of DMF as the solvent, the PbI_2 and FAI are added, and in the case of 2-Me and FAAc as the solvent, the PbI_2 and FAI are added. The concentrations of these solutes are set to be comparable with the cases in our experiments. The solutes and solvent are first randomly generated in the simulation box, after which a 10^6 MD steps (6 ns) simulation is empolyed for system

equilibration and another 10^6 MD steps simulation are used for data analysis. Dozens of parallel simulations with different initial particle configurations are performed to obtain the final results.

Characterizations and measurements

Perovskite precursor solution characterizations

Fourier Transform Infrared (FTIR) spectroscopy was characterized by FT/IR6100 (Jasco).

Proton nuclear magnetic resonance (NMR) spectra were measured with a JOEL NMR spectrometer (JNM-ECZ400S, 400 MHz Japan).

Dynamic light scattering (DLS) experiments were performed using a Malvern Zetasizer Nano instrument.

Zeta potential measurements were performed using a Malvern Zetasizer Nano instrument.

Thermal Gravimetric (TG) measurements were performed using a Mettler Toledo TGA 2(SF).

Perovskite thin film characterizations

Scanning electron microscopy (SEM) analysis was performed on a SU8010 electron microscope. SEM images were captured using a 5-kV acceleration voltage and an aperture size of 20 μm.

Grazing-incidence wide-angle X-ray scattering (GIWAXS) was performed at the BL14BL beamline of the Shanghai Synchrotron Radiation Facility (SSRF) using X-ray with a wavelength of 1.24 Å. The α-$FAPbI_3$ (100) reflection at $q_z = 9.6$ nm^{-1}, the δ phase at $q_z = 8.1$ nm^{-1}, and the PbI_2 at $q_z = 8.8$ nm^{-1}. These assignments are consistent with reported literature values and are used to track the phase evolution during crystallization.

Steady-state photoluminescence (PL) spectra and Time-resolved photoluminescence (TRPL) spectra were obtained by FLS1000. The excitation wavelength was set as 520 nm. The TRPL decay data were modeled by a biexponential formula: $Y+A1\exp(-t/\tau1) +A2\exp(-t/\tau2)$.

The in-situ PL measurements were initiated at 20 °C. The sample-stage temperature was then ramped from 20 °C to 145 °C to induce thermal annealing, and this temperature was subsequently maintained throughout the measurement.

X-ray diffraction (XRD) patterns were performed using Cu Kα radiation as the X-ray source by a Smart Lab diffractometer from Japan.

Device characterizations

Transient photocurrent (TPC) measurement was performed with a system excited by a 532 nm (1000 Hz, 3.2 ns) pulse laser. A shorter TPC decay lifetime (τ_{TPC}) indicates faster carrier transport and more efficient charge extraction with reduced trapping, supporting the improved device performance. The TPC decay lifetime (τ_{TPC}) is extracted by exponential fitting of the transient current using

$$I(t) = I_0 \exp(-t/\tau_{TPC}).$$

Transient photovoltage (TPV) measurement was performed with the same 5 system excited by a 405 nm (50 Hz, 20 ms) pulse laser. A digital oscilloscope (Tektronix, D4105) was used to record the photocurrent or photovoltage decay process with a sampling resistor of 50 Ω or 1 MΩ, respectively. Transient photovoltage (TPV) measurements are performed under open-circuit conditions to probe charge recombination dynamics. After a small light perturbation, the decay of the photovoltage reflects the carrier recombination lifetime. A longer τ_{TPV} indicates suppressed non-radiative recombination and reduced trap-assisted losses. The TPV lifetime (τ_{TPV}) is obtained by exponential fitting of the voltage decay using

$$V(t)=V_0 \exp(-t/\tau_{TPV}).$$

Photo current-voltage (J-V) curves were measured by using 2400 Series Source Meter (Keithley Instruments) under a SS-F5-3A solar simulator (AM 1.5G, 100 mW cm^{-2}) (Enlitech) calibrated by a NREL standard Si cell, and no additional UV filter equipment was used. The measurements were carried out with the devices inside the glove box (<0.1 ppm O_2 and H_2O) To ensure the accuracy of the Jsc measured from JV scans, a mask with an aperture area of 0.1 cm^2 was covered during the measurement. The J-V curves were scanned by reverse (forward bias (1.3 V) → short circuit (-0.2 V)) scan with scan rate of 50 mVs^{-1}, and 1 ms delay time.

Mini-module device photo J-V curves were measured by using the same Instruments. The J-V curves were scanned by reverse (forward bias (7.3 V) → short circuit (-0.2 V)) scan with scan rate of 100 mVs^{-1}, and 1 ms delay time. The measurements were carried out in the glove box (<0.1 ppm O_2 and H_2O). We designed an etching pattern with an active area of 12.6 cm^2 (Fig. S19, S20). A laser system was used to precisely etch the P1, P2, and P3 channels, ensuring

the accuracy and consistency of the active area.

Stability tests

The long-term stability characterization, the devices were placed in a nitrogen glove box at room temperature (dark environment). Photocurrent density-voltage (J-V) curves were measured in an N_2-filled glovebox using a Keithley 2400 source meter under a simulated AM1.5G spectrum and a Xenon arc lamp based solar simulator (Enli Tech, Taiwan). The operational stability measurements (MPP tracking) were performed with a multi-channel thin film photovoltaic attenuation test system under a LED lamp which was adjusted to adjusted to simulate the AM1.5G solar spectrum with a standard light intensity (100 mW cm^{-2}) (Suzhou D&RInstrument Co., Ltd., PVLT 6001M-16A). The devices were masked (12.6 cm^2) and were measured with a resistive load tracking routine under continuous 1 sun illumination in ambient air with a relative humidity of 25 ± 5%. The temperature of the device and the glove box is kept at about 65 °C and the temperature is reduced by continuous circulation of condensed water.

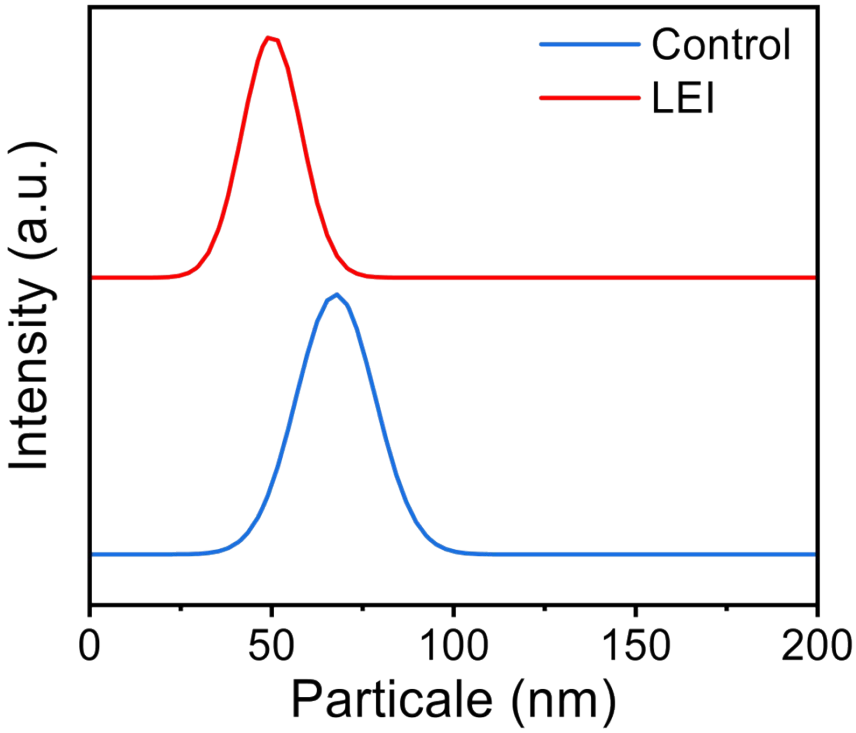

Fig. S1 Control ink and LEI perovskite precursor micelle size distribution.

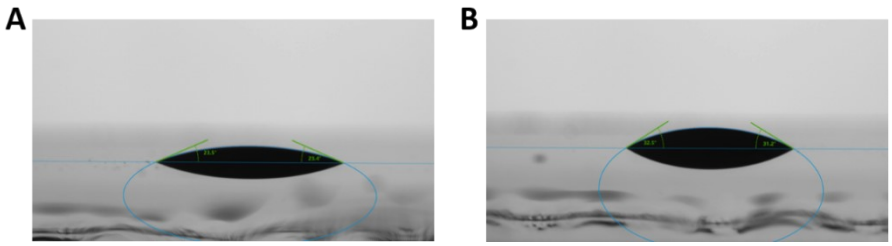

Fig. S2 The contact angle of perovskite precursors based on (A) LEI and (B) Control ink.

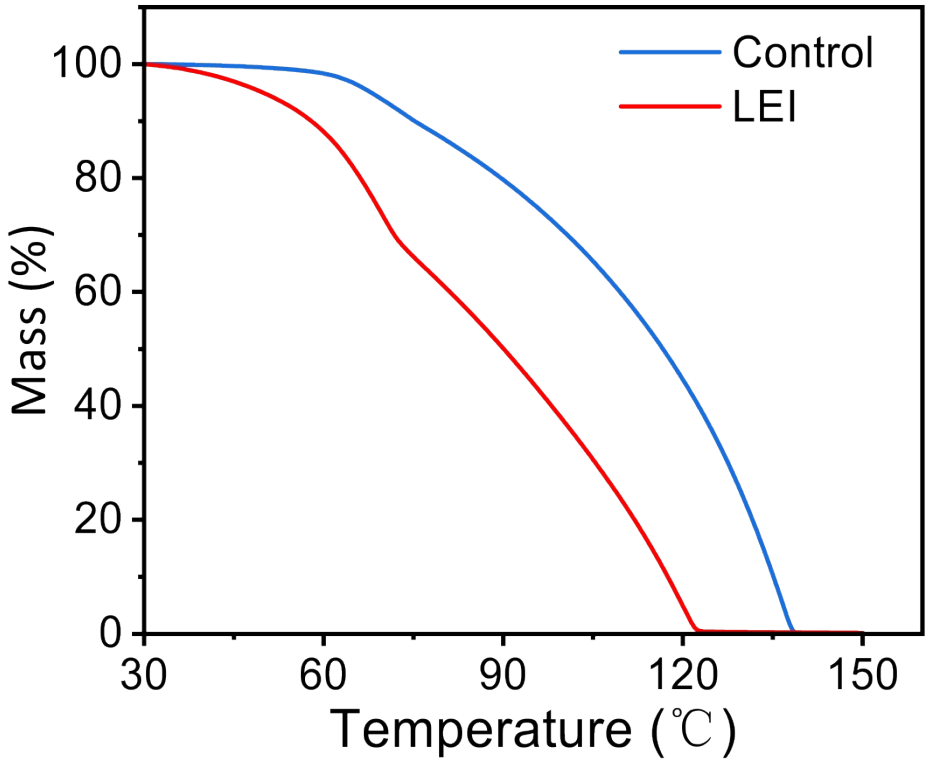

Fig. S3 The drying temperatures of control ink and IEL by TGA measurement.

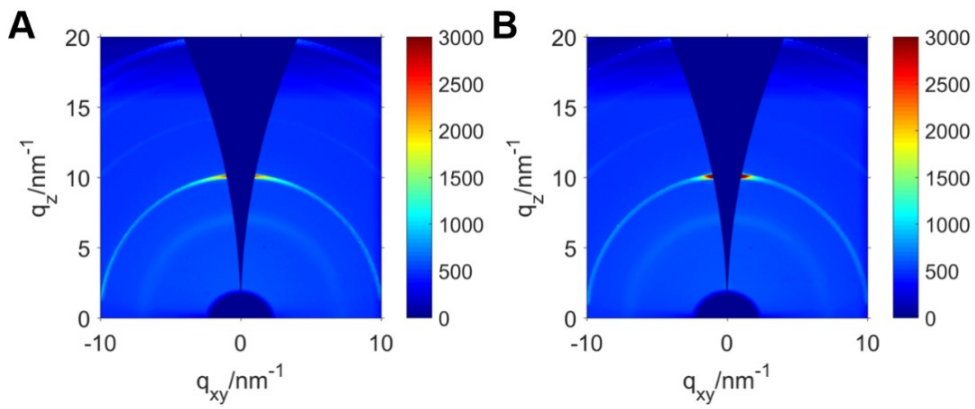

Fig. S4 2D GIWAXS pattern of perovskite thin films based on (A) Control ink and (B) LEI.

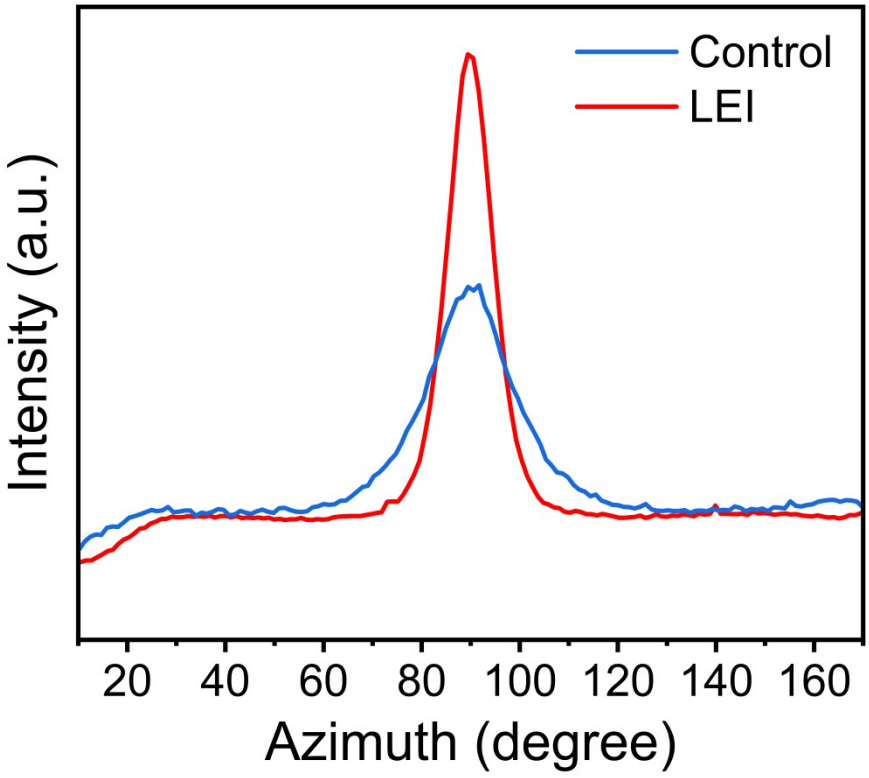

Fig. S5 The integral of the azimuth Angle of the (100) crystal plane from the GIWAXS pattern.

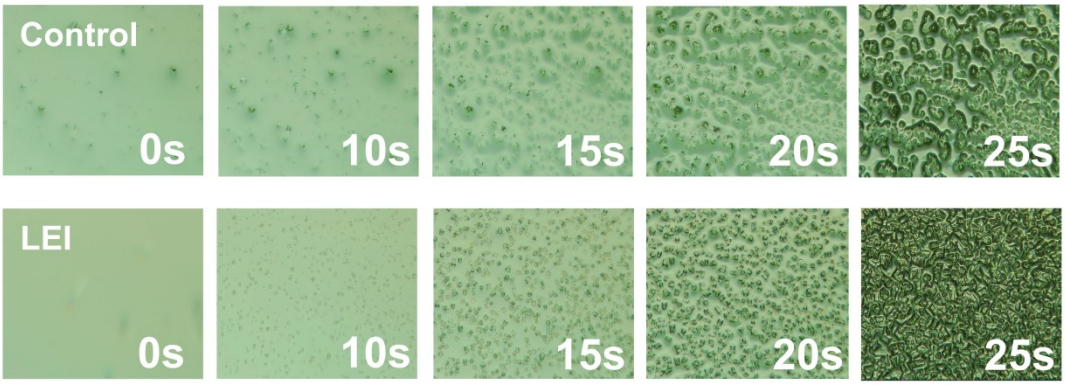

Fig. S6 Optical microscope photos of natural drying of different inks.

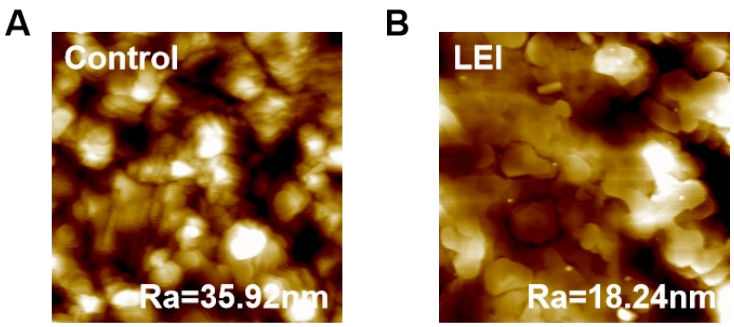

Fig. S7 AFM images of perovskite films based on (A) Control ink and (B) LEI.

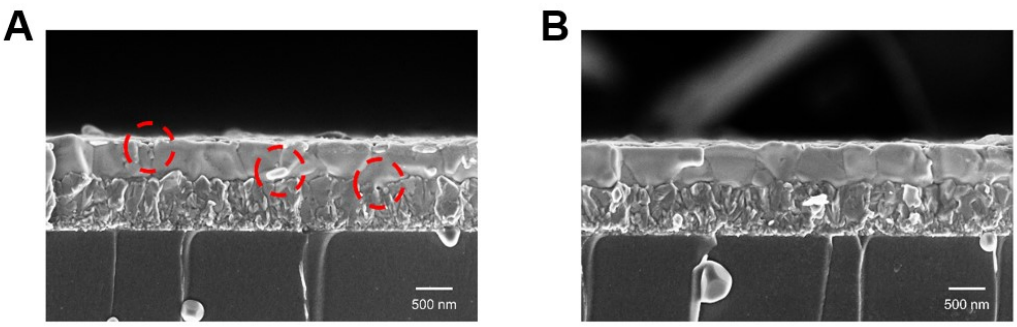

Fig. S8 Cross-sectional SEM images of perovskite films based on (A) Control ink and (B) LEI.

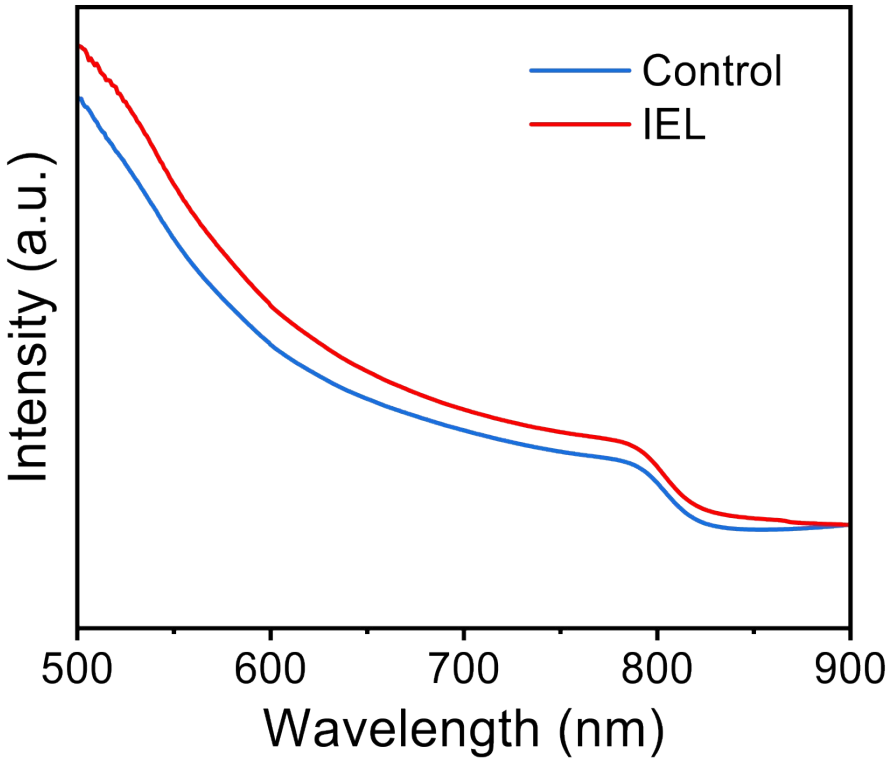

Fig. S9 UV–Vis absorption spectra of perovskite films prepared with Control ink and LEI.

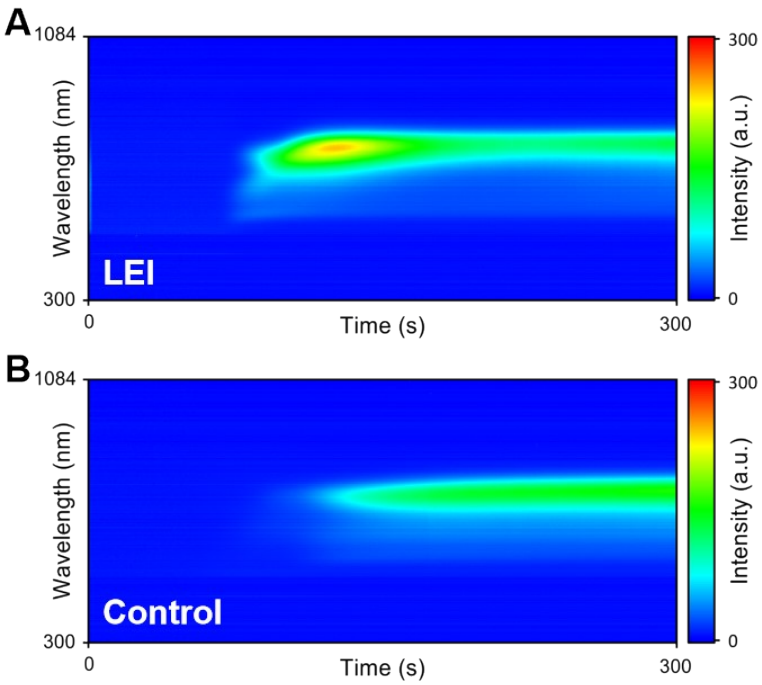

Fig. S10 In-situ PL spectrum of the perovskite thin films based on (A) LEI and (B) Control ink during natural drying.

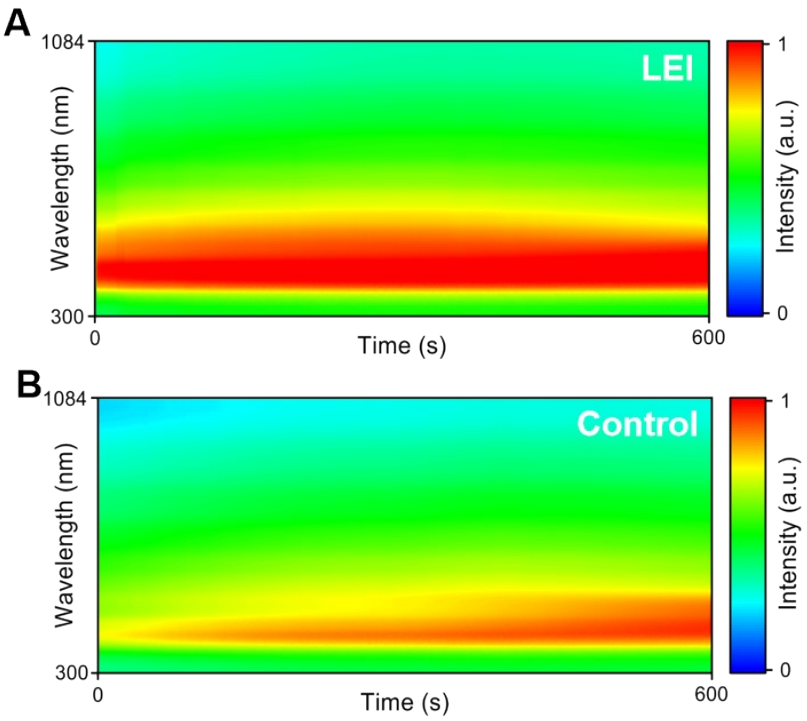

Fig. S11 In-situ UV-Vis absorption spectrum of the perovskite thin films based on (A) LEI and (B) Control ink during natural drying.

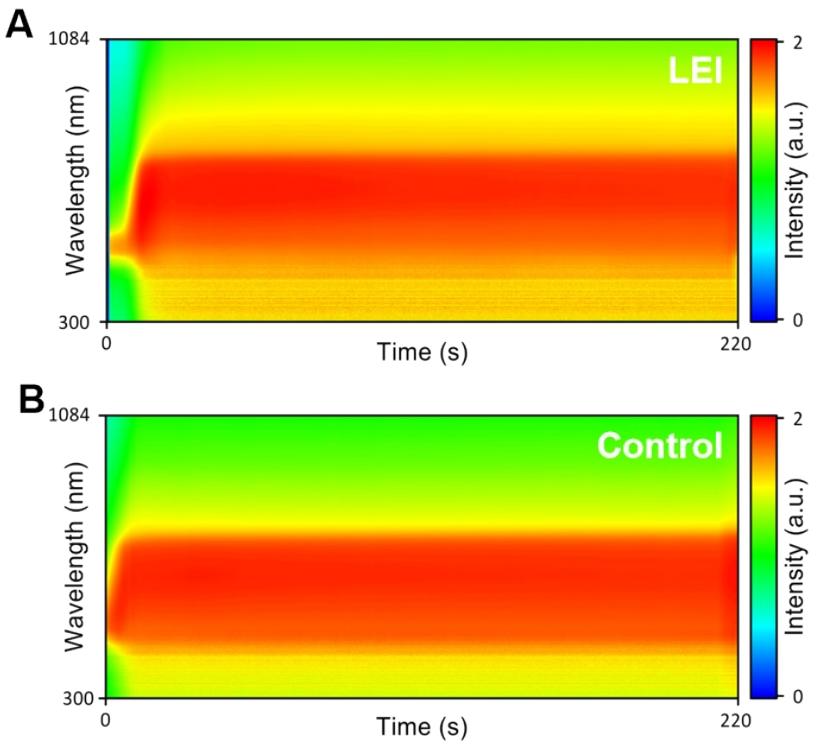

Fig. S12 In-situ UV-Vis absorption spectrum of the perovskite films based on (A) LEI and (B) Control during annealing stage.

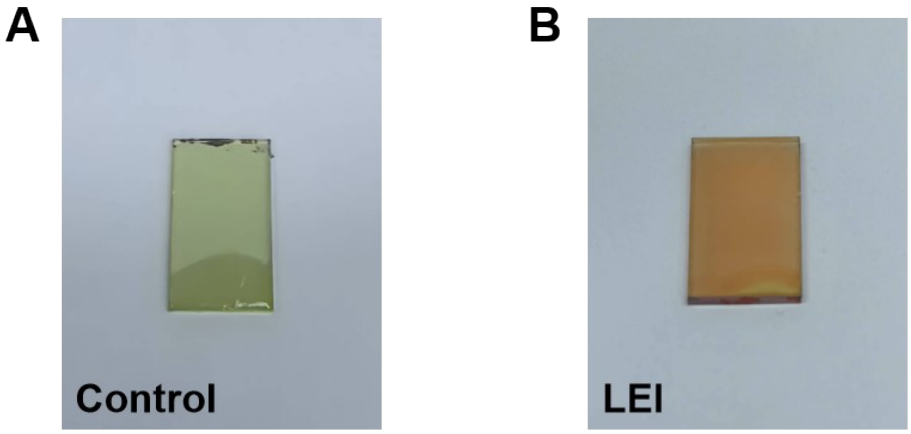

Fig. S13 Photos of color changes of (A) Control (B) LEI based perovskite thin films.

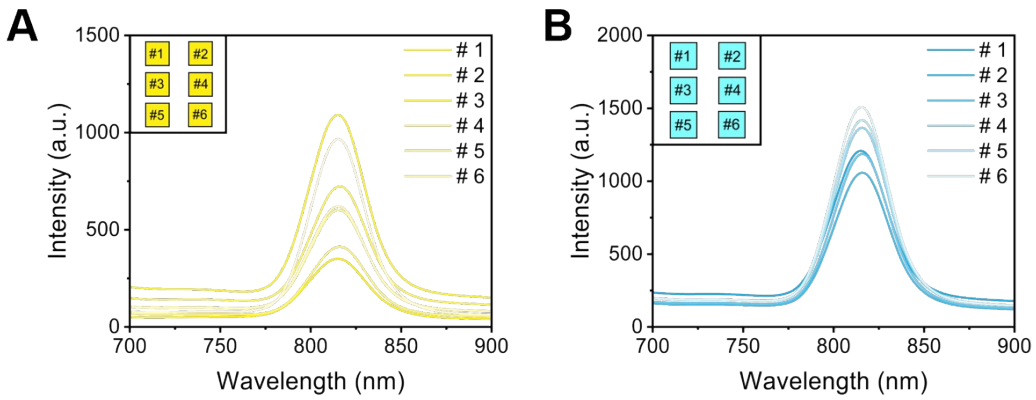

Fig. S14 PL spectra of perovskite films of (A) Control, (B) LEI based perovskite films.

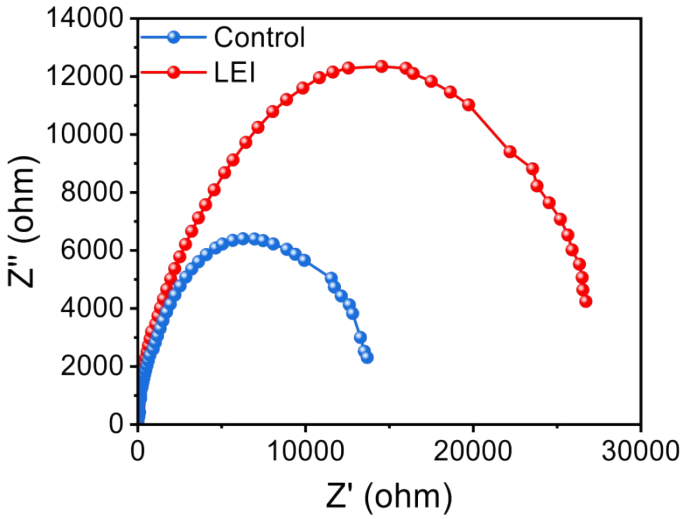

Fig. S15 Nyquist plot of the impedance spectra of Control and LEI-based PSCs.

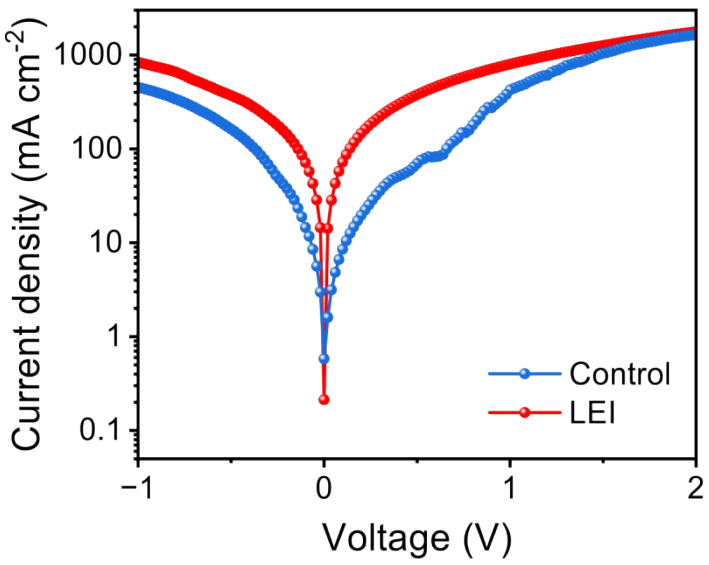

Fig. S16 Dark J-V curves of the control and LEI-based devices.

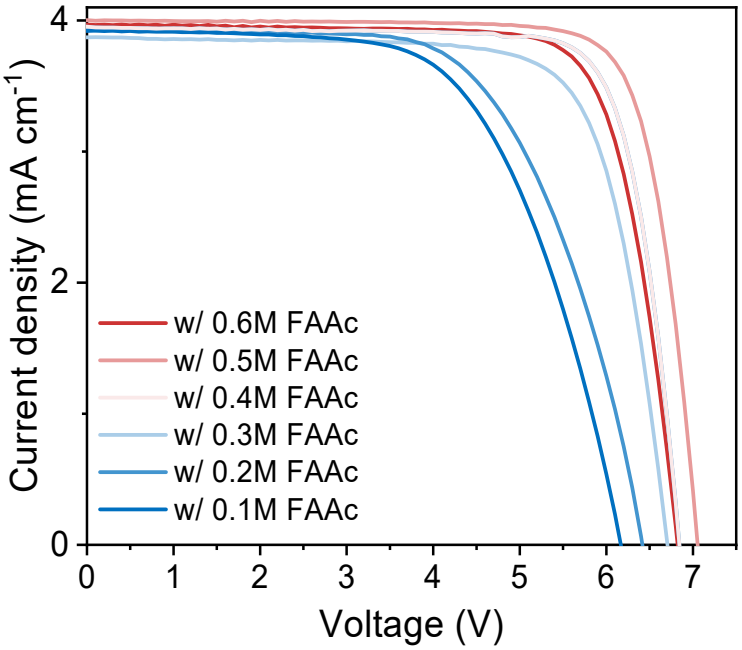

Fig. S17 Effect of FAAc concentration in LEI on device performance.

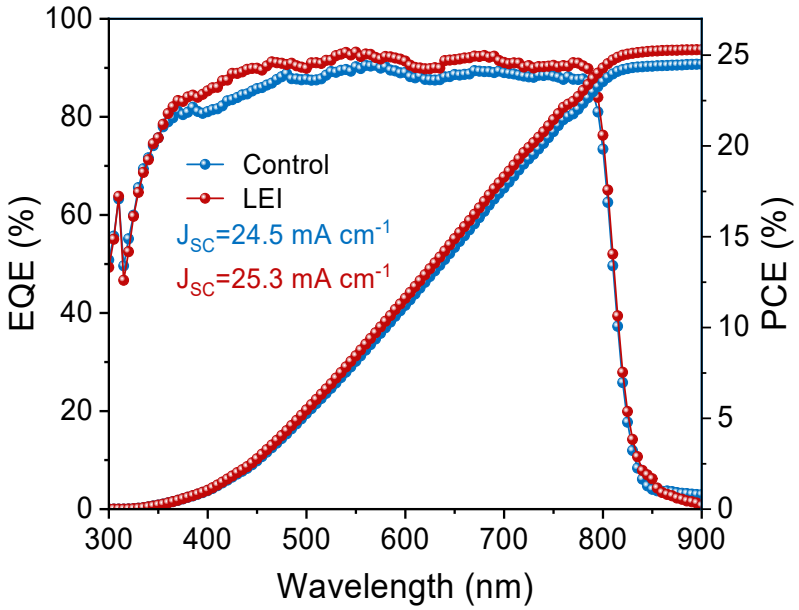

Fig. S18 External quantum efficiency (EQE) spectra of the PSCs for Control and LEI devices.

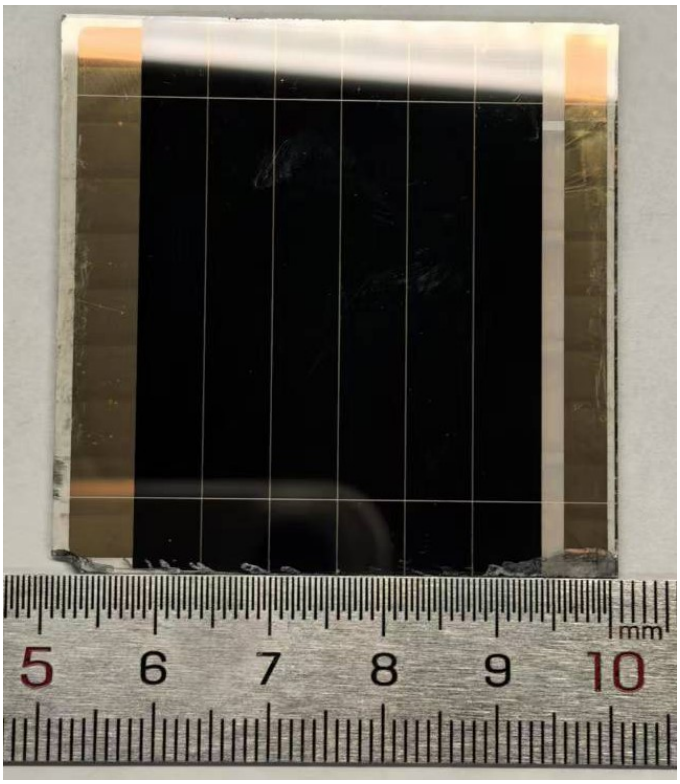

Fig. S19 Photo of PSMs with an active area of 12.6 cm^2 and 6 sub-cells connected in series.

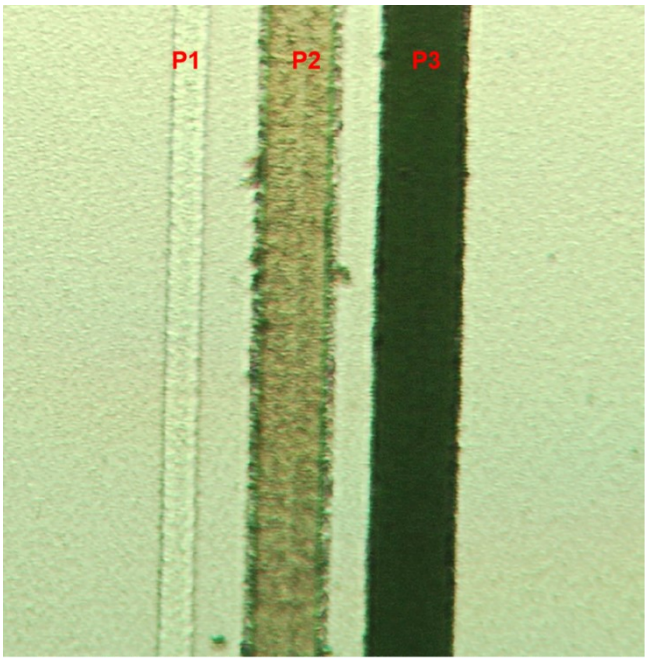

Fig. S20 Schematic of the P1, P2, and P3 regions in the PSMs.

检 验 检 测 结 果
Test Results

序号 Clause	检验项目 Test item(s)	单位 Unit	技术要求 Technical requirements	结果 Results	单项评价 Verdict Pass/Fail
2	电流-电压特性的测量 (反扫) Current-voltage characteristic measurement (Reverse Scan)	—	在标准试验条件下（样品温度：25℃±2℃，辐照度：1000W/ m²，标准太阳光谱辐照分布符合 IEC 60904-3 规定），测量样品随负荷变化的电流-电压特性。 At STC (module temperature: 25℃±2℃, irradiance: 1000W/m², standard solar spectral irradiance distribution corresponds to IEC60904-3), measure the current-voltage characteristics of the cell with the variation of load.	—	—
2.1	开路电压 Voc Open-circuit voltage, Voc	V	—	7.029	—
2.2	短路电流 Isc Short-circuit current, Isc	mA	—	49.00	—
2.3	最大功率 Pmax Maximum-power, Pmax	mW	—	266.8	—
2.4	最大功率点电压 Vmp Maximum-power voltage, Vmp	V	—	5.900	—
2.5	最大功率点电流 Imp Maximum-power current, Imp	mA	—	45.22	—
2.6	填充因子 FF，% Fill factor FF, %	—	—	77.46	—
2.7	转换效率 η，% Conversion efficiency η, %	—	$\eta = \frac{P_{max}}{1000W/m^2 \times S} \times 100\%$ S 为掩膜板面积/Area S is determined by mask	21.76	—

备注：反扫扫描方向为 7.2V~-0.2V，步进-0. 1V，延迟时间：1s；短路电流密度$J_{sc} = \frac{I_{sc}}{S}$ =3.997 mA/cm²。
计算短路电流密度及转换效率所用面积为掩膜板面积，S=12.26 cm²。
Remark: Reverse sweep direction: 7.2V~-0.2 V, step: -0.1V, delay time: 1s. $J_{sc} = \frac{I_{sc}}{S}$ =3.997 mA/cm²
The area used to calculate J_{sc} and Conversion efficiency is determined by mask, S=12.26 cm².

Fig. S21 Reverse-scan characteristics of photovoltaic cells certified by an accredited third-party laboratory (IEC 60904-1 2022 standard).

检 验 检 测 结 果
Test Results

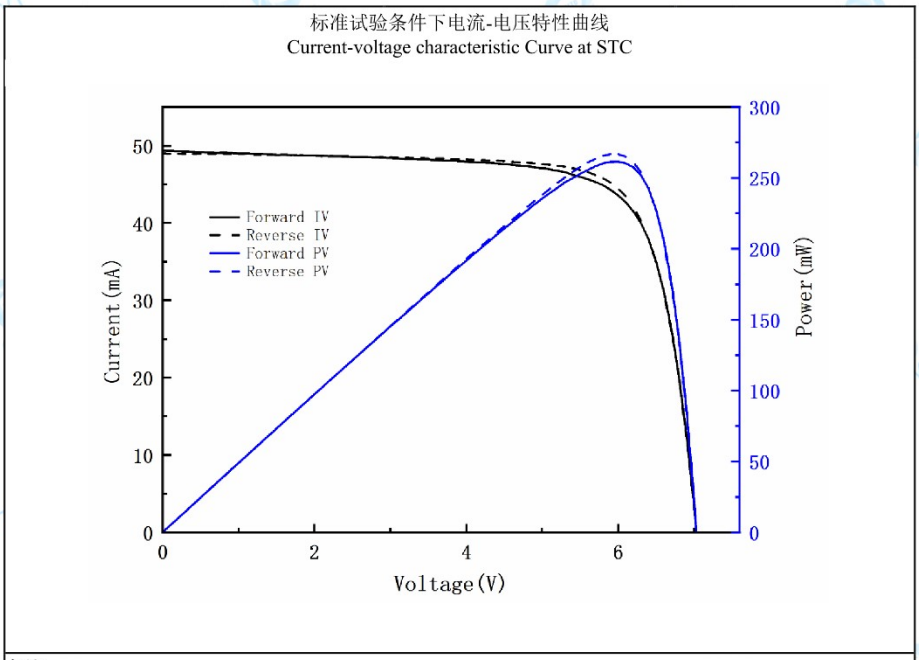

备注：—
Remark: —

Fig. S22 Current-voltage characteristic Curve at STC (IEC 60904-1 2022 standard).

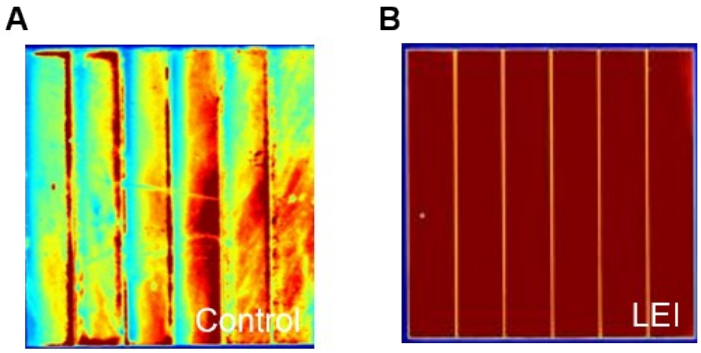

Fig. S23 PL mapping images of 5 × 5 cm^2 perovskite solar modules of the control ink (A) and the LEI (B).

Table S1 Boiling point, saturated vapor pressure and DN value of different solvents.

	BP (℃)	SVP (kPa, 25 ℃)	DN (kcal/mol)
DMF	153	0.36	26.6
2-Me	124	1.3	19.3
MeOH	64.7	16.9	19.0
EtOH	78.4	5.95	19.2
IPA	82.6	4.4	18.0

Table S2 Detail data of symmetric-adapted perturbation theory.

Species	Electrostatics (Kcal/mol)	Exchange (Kcal/mol)	Induction (Kcal/mol)	Dispersion (Kcal/mol)	Total (Kcal/mol)
Ac^-+2-Me	-30.49	29.87	-16.89	-8.48	-25.99
FA^+ +2-Me	-21.50	19.66	-11.76	-4.50	-18.10

Table S3 Performance of PSCs (0.049 cm^2) based on different inks.

	V_{OC} (V)	J_{SC} (mA cm^{-2})	FF (%)	PCE (%)
Control	1.12	25.57	75.84	21.68
LEI	1.18	25.38	81.65	25.23

Table S4 Reported PCE Statistics of MA^+-Free, and Cs^+-Free Perovskite Solar Cells (PSCs) and Modules (PSMs).

Process	Devices	V_{OC} (V)	J_{SC} (mA cm^{-2})	FF (%)	PCE (%)
Spin-coating	PSCs	1.13	26.25	81.2	24.1[15]
Spin-coating	PSCs	1.12	24.85	83.29	23.14[16]
	PSMs ($13.8cm^2$)	6.61	3.76	74.18	18.43[16]
Spin-coating	PSCs	1.14	25.99	78.15	23.15[17]
	PSMs ($12.6cm^2$)	6.69	4.14	65.56	19.66[17]
Spin-coating	PSCs	1.03	23.55	78	18.83[18]
Spin-coating	PSCs	1.10	25.50	77	21.6[19]
Spin-coating	PSCs	1.07	24.90	75.4	20.19[20]
Spin-coating	PSCs	1.10	24.79	81.50	22.22[21]
Spin-coating	PSCs	1.06	25.90	76.45	21.05[22]
Blade-Coating （our work）	PSCs	1.18	26.43	80.58	25.23
	PSMs ($12.6cm^2$)	7.01	4.08	80.49	23.05

Table S5 Performance of PSMs (12.6 cm^2) based on different inks.

	V_{OC} (V)	J_{SC} (mA cm^{-2})	FF (%)	PCE (%)
Control	6.58	3.94	73.31	19.04
LEI	7.01	4.08	80.49	23.05

References

1. Z. D. Wang, S. Liang, Y. Q. Yang, Z. N. Liu, X. Z. Duan, X. P. Li, T. B. Liu and H. Y. Zang, *Nature Communications*, 2023, **14**.
2. L. Yao, C. Lin, X. Duan, X. Ming, Z. Chen, H. Zhu, S. Zhu and Q. Zhang, *Nature Communications*, 2023, **14**, 6563.
3. B. Liu, B. Hu, J. Du, D. Cheng, H.-Y. Zang, X. Ge, H. Tan, Y. Wang, X. Duan, Z. Jin, W. Zhang, Y. Li and Z. Su, *Angewandte Chemie International Edition*, 2021, **60**, 6076–6085.
4. B. Li, X. Z. Duan, D. M. Cheng, X. Y. Chen, Z. X. Gao, W. B. Ren, K. Z. Shao and H. Y. Zang, *Journal of the American Chemical Society*, 2023, **145**, 2243–2251.
5. C. Wang, X. Z. Duan, Y. Jiang, Q. Q. Liu, J. X. Ma, Z. M. Su and H. Y. Zang, *Advanced Materials*, 2025, **37**.
6. X. Z. Duan, A. C. Shi and L. J. An, *Macromolecules*, 2021, **54**, 9053–9062.
7. H. Y. Huo, W. C. Zhao, X. Z. Duan and Z. Y. Sun, *Macromolecules*, 2023, DOI: 10.1021/acs.macromol.2c01780.
8. J. C. Liang, H. Wei, K. F. Yu, C. J. Lin, H. F. Li, M. M. Ding and X. Z. Duan, *Soft Matter*, 2021, **17**, 6305–6314.
9. L. F. Chao, Y. D. Xia, X. Z. Duan, Y. Wang, C. X. Ran, T. T. Niu, L. Gu, D. L. Li, J. F. Hu, X. Y. Gao, J. Zhang and Y. H. Chen, *Joule*, 2022, **6**, 2203–2217.
10. M. Y. Chen, T. T. Niu, L. F. Chao, X. Z. Duan, J. P. Wang, T. F. Pan, Y. J. Li, J. H. Zhang, C. Y. Wang, B. Y. Ren, L. J. Guo, M. Hatamvand, J. Zhang, Q. X. Guo, Y. D. Xia, X. Y. Gao and Y. H. Chen, *Energy & Environmental Science*, 2024, **17**, 3375–3383.
11. B. Li, X. Z. Duan, Y. Z. Cui, T. Li, X. Y. Chen, Q. Q. Liu, X. Liu, Y. X. Meng, W. B. Ren, L. Y. Wang, S. Liang and H. Y. Zang, *Angewandte Chemie-International Edition*, 2024, **63**.
12. S. J. Marrink, H. J. Risselada, S. Yefimov, D. P. Tieleman and A. H. de Vries, *The Journal of Physical Chemistry B*, 2007, **111**, 7812–7824.
13. S. Plimpton, *Journal of Computational Physics*, 1995, **117**, 1–19.

14. K. J. Oh, G. T. Gao and X. C. Zeng, *Physical Review Letters*, 2001, **86**, 5080–5083.
15. Y. Zhang, Y. Chen, G. Liu, Y. Wu, Z. Guo, R. Fan, K. Li, H. Liu, Y. Zhao, T. Kodalle, Y. Chen, C. Zhu, Y. Bai, Q. Chen and H. Zhou, *Science*, 2025, **387**, 284–290.
16. T. Niu, L. Chao, Y. Xia, K. Wang, X. Ran, X. Huang, C. Chen, J. Wang, D. Li, Z. Su, Z. Hu, X. Gao, J. Zhang and Y. Chen, *Advanced Materials*, 2024, **36**, 2309171.
17. J. Liu, J. Cao, M. Zhang, X. Sun, T. Hou, X. Yang, L. Xiang, X. Liu, Z. Fu, Y. Huang, F. Wang, W. Zhang and X. Hao, *Advanced Science*, 2024, **11**, 2410266.
18. K. M. M. Salim, S. Masi, A. F. Gualdrón-Reyes, R. S. Sánchez, E. M. Barea, M. Krecmarová, J. F. Sánchez-Royo and I. Mora-Seró, *ACS Energy Lett*, 2021, **6**, 3511–3521.
19. T. Du, T. J. Macdonald, R. X. Yang, M. Li, Z. Jiang, L. Mohan, W. Xu, Z. Su, X. Gao, R. Whiteley, C.-T. Lin, G. Min, S. A. Haque, J. R. Durrant, K. A. Persson, M. A. McLachlan and J. Briscoe, *Advanced Materials*, 2022, **34**, 2107850.
20. D. Lin, Y. Gao, T. Zhang, Z. Zhan, N. Pang, Z. Wu, K. Chen, T. Shi, Z. Pan and P. Liu, *Advanced Functional Materials*, 2022, **32**.
21. Y. Zhang, Y. Li, L. Zhang, H. Hu, Z. Tang, B. Xu and N.-G. Park, *Advanced Energy Materials*, 2021, **11**, 2102538.
22. D. Wang, M. Chen, X. Zhang, L. Chao, T. Niu, Y. Lv, G. Xing, Y. Xia, M. Li, H. Zhang and Y. Chen, *ACS Applied Materials & Interfaces*, 2023, **15**, 16818–16827.